

---

*This copy is for your personal, non-commercial use only.*

---

If you wish to distribute this article to others, you can order high-quality copies for your colleagues, clients, or customers by [clicking here](#).

Permission to republish or repurpose articles or portions of articles can be obtained by following the guidelines [here](#).

**The following resources related to this article are available online at [www.sciencemag.org](http://www.sciencemag.org) (this information is current as of February 17, 2011):**

**Updated information and services**, including high-resolution figures, can be found in the online version of this article at:

<http://www.sciencemag.org/content/301/5640/1698.full.html>

This article has been **cited by** 328 article(s) on the ISI Web of Science

This article has been **cited by** 20 articles hosted by HighWire Press; see:

<http://www.sciencemag.org/content/301/5640/1698.full.html#related-urls>

This article appears in the following **subject collections**:

Chemistry

<http://www.sciencemag.org/cgi/collection/chemistry>

(such as rapid strong anisotropy variations with the radius), but the orbit library analysis rules out this possibility for NGC 3379, and in general such behavior has not been found in detailed modeling of elliptical galaxies. Latent disks could be the explanation, but as with NGC 3379, the observed rotational speeds are low, and hiding them adequately would require coincidentally unpropitious viewing angles. Thus, it seems most plausible that the apparent Keplerian decline in the velocity dispersions of all of these systems is accurate, and many ordinary elliptical galaxies are highly deficient in dark matter relative to other galaxy types—a possibility already suggested by previous dynamical studies (21, 26, 27).

This result clashes with conventional conceptions of galaxy formation. In particular, if ellipticals are built up by mergers of smaller galaxies, it is puzzling that the resulting systems show little trace of their precursors' dark matter halos. More detailed comparisons with the predictions of the standard CDM paradigm are not yet possible, because the baryonic processes during galaxy formation are complex, and high-resolution *ab initio* simulations are so far unable to reproduce an elliptical galaxy. However, estimating the effects of a baryonic collapse on a CDM halo (28) with an adiabatic approximation yields  $Y_{B5} \sim 20$ . Low-resolution simulations including baryonic processes (29), extrapolated inward in radius, also predict  $Y_{B5} \sim 20$ . These values conflict with those derived for the observed galaxies above. However, CDM predictions at the virial radius are generally supported by statistical studies of  $L^*$  ellipticals with weak gravitational lensing (30). This apparent disparity could be resolved if the dark matter content of ellipticals varies, or if these galaxies have large amounts of dark matter spread out to still larger radii than the PNs can probe. The former scenario requires a suitable mechanism for dark matter depletion, and the latter violates CDM predictions for high central concentrations of dark halos—a problem that is also increasingly evident in other stellar systems (31).

It is apparent that some important physics is still missing from the recipes for galaxy formation. For example, substantial portions of these galaxies' dark matter halos could have been shed through interactions with other galaxies. Such stripping has been inferred for ellipticals near the centers of dense galaxy clusters (32), but the galaxies we studied here are in much sparser environments, in which we do not expect substantial stripping to be an important process. Crucial to understanding the incidence and origin of this low-dark matter phenomenon will be the results for a large sample of ellipticals with a broad range of properties, including differing environmental densities, which could be a key factor in determining halo outcomes; the continuing P.N.S. observing program will provide this sample.

# References and Notes

1. M. Persic, P. Salucci, F. Stel, *Mon. Not. R. Astron. Soc.* **281**, 27 (1996).
2. M. Loewenstein, R. E. White III, *Astrophys. J.* **518**, 50 (1999).
3. C. R. Keeton, *Astrophys. J.* **561**, 46 (2001).
4. J. Kley, M. I. Wilkinson, N. W. Evans, G. Gilmore, C. Frayn, *Mon. Not. R. Astron. Soc.* **330**, 792 (2002).
5. D. S. Madgwick et al., *Mon. Not. R. Astron. Soc.* **333**, 133 (2002).
6. A. Kronawitter, R. P. Saglia, O. Gerhard, R. Bender, *Astron. Astrophys. Suppl. Ser.* **144**, 53 (2000).
7. X. Hui, H. C. Ford, K. C. Freeman, M. A. Dopita, *Astrophys. J.* **449**, 592 (1995).
8. N. G. Douglas et al., *Publ. Astron. Soc. Pac.* **114**, 1234 (2002).
9. R. Ciardullo, G. H. Jacoby, H. B. Dejonghe, *Astrophys. J.* **414**, 454 (1993).
10. J. Magorrian, D. Ballantyne, *Mon. Not. R. Astron. Soc.* **322**, 702 (2001).
11. Methods are available as supporting material on Science Online.
12. R. Jedrzejewski, P. L. Schechter, *Astron. J.* **98**, 147 (1989).
13. T. S. Statler, T. Smecker-Hane, *Astrophys. J.* **117**, 839 (1999).
14. R. Bender, R. P. Saglia, O. E. Gerhard, *Mon. Not. R. Astron. Soc.* **269**, 785 (1994).
15. N. A. Bahcall, L. M. Lubin, *Astrophys. J.* **447**, L81 (1995).
16. A. J. Romanowsky, C. S. Kochanek, *Astrophys. J.* **553**, 722 (2001).
17. M. Capaccioli, E. V. Held, H. Lorenz, M. Vietri, *Astron. J.* **99**, 1813 (1990).
18. H.-W. Rix, C. M. Carollo, K. Freeman, *Astrophys. J.* **513**, L25 (1999).
19. T. S. Statler, *Astron. J.* **121**, 244 (2001).
20. M. A. Beasley et al., in preparation.
21. O. Gerhard, A. Kronawitter, R. P. Saglia, R. Bender, *Astron. J.* **121**, 1936 (2001).
22. K. Gebhardt et al., *Astron. J.* **119**, 1157 (2000).
23. S. E. Schneider et al., *Astron. J.* **97**, 666 (1989).
24. R. H. Méndez et al., *Astrophys. J.* **563**, 135 (2001).
25. H.-W. Rix, P. T. de Zeeuw, N. Cretton, R. P. van der Marel, C. M. Carollo, *Astrophys. J.* **488**, 702 (1997).
26. G. Bertin et al., *Astron. Astrophys.* **292**, 381 (1994).
27. M. Capaccioli, N. R. Napolitano, M. Arnaboldi, in *Proc. Sakharov Conf. Phys.*, in press (available on <http://xxx.lanl.gov/abs/astro-ph/0211323>).
28. J. F. Navarro, C. S. Frenk, S. D. M. White, *Astrophys. J.* **490**, 493 (1997).
29. D. H. Weinberg, R. Davé, N. Katz, L. Hernquist, *Astrophys. J.*, in press (available on <http://xxx.lanl.gov/abs/astro-ph/0212356>).
30. G. Wilson, N. Kaiser, G. A. Luppino, L. L. Cowie, *Astrophys. J.* **555**, 572 (2001).
31. J. P. Ostriker, P. Steinhardt, *Science* **300**, 1909 (2003).
32. P. Natarajan, J.-P. Kneib, I. Smail, *Astrophys. J.* **580**, L11 (2002).
33. J. L. Tonry et al., *Astrophys. J.* **546**, 681 (2001).
34. G. de Vaucouleurs et al., *Third Reference Catalogue of Bright Galaxies* (Springer-Verlag, New York, 1991).
35. S. M. Faber et al., *Astrophys. J. Suppl. Ser.* **69**, 763 (1989).
36. G. H. Jacoby, R. Ciardullo, W. E. Harris, *Astrophys. J.* **462**, 1 (1996).
37. This work is based on observations made with the William Herschel Telescope operated on the island of La Palma by the Isaac Newton Group in the Spanish Observatorio del Roque de los Muchachos of the Instituto de Astrofísica de Canarias. We used the HyperLeda galaxy database, which is available on [www-obs.univ-lyon1.fr/hypercat](http://www-obs.univ-lyon1.fr/hypercat). We thank O. Gerhard and the anonymous referee for their helpful comments for improving the paper. N.R.N. is supported by the European Commission FP5 Marie Curie Fellowships Programme.

## Supporting Online Material

[www.sciencemag.org/cgi/content/full/1087441/DC1](http://www.sciencemag.org/cgi/content/full/1087441/DC1)  
Materials and Methods  
Figs. S1 to S5  
References

30 May 2003; accepted 19 August 2003  
Published online 28 August 2003;  
10.1126/science.1087441  
Include this information when citing this paper.

# Ultrafast Hydrogen-Bond Dynamics in the Infrared Spectroscopy of Water

C. J. Fecko,<sup>1,2\*</sup> J. D. Eaves,<sup>1,2\*</sup> J. J. Loparo,<sup>1,2</sup>  
A. Tokmakoff,<sup>1,2†</sup> P. L. Geissler<sup>1‡</sup>

We investigated rearrangements of the hydrogen-bond network in water by measuring fluctuations in the OH-stretching frequency of HOD in liquid D<sub>2</sub>O with femtosecond infrared spectroscopy. Using simulations of an atomistic model of water, we relate these frequency fluctuations to intermolecular dynamics. The model reveals that OH frequency shifts arise from changes in the molecular electric field that acts on the proton. At short times, vibrational dephasing reflects an underdamped oscillation of the hydrogen bond with a period of 170 femtoseconds. At longer times, vibrational correlations decay on a 1.2-picosecond time scale because of collective structural reorganizations.

The properties of liquid water that govern processes such as aqueous solvation and the transport of protons arise from the motions

of water molecules within a constantly changing network of hydrogen bonds. The dynamics of this network occur over a range of time scales, from femtosecond fluctuations that involve a few molecules to picosecond diffusive motions that involve the breaking and forming of hydrogen bonds (1–7). Time-resolved infrared (IR) spectroscopy is an ideal technique to investigate these dynamics, because the frequency of the intramolecular OH stretching

<sup>1</sup>Department of Chemistry, <sup>2</sup>George R. Harrison Spectroscopy Laboratory, Massachusetts Institute of Technology (MIT), Cambridge, MA 02139, USA.

\*These authors contributed equally to this work.

†To whom correspondence should be addressed. E-mail: [tokmakoff@mit.edu](mailto:tokmakoff@mit.edu)

‡Present address: Department of Chemistry, University of California, Berkeley, CA 94720, USA.

vibration is particularly sensitive to a molecule's hydrogen-bond environment. Relative to the gas phase, this frequency red-shifts and the line shape broadens significantly because of hydrogen bonding in the liquid (Fig. 1A). Therefore, time-dependent shifts in the OH vibrational frequency, or spectral diffusion, can characterize changes in hydrogen bonding and intermolecular configuration. Previous time-resolved IR studies have concentrated on time scales from a few hundred femtoseconds to several picoseconds (8–13), but have lacked sufficient time resolution to investigate the dynamics on the shorter time scales observed in femtosecond optical spectroscopies and predicted from simulation. Additionally, interpreting dynamics observed in IR experiments in terms of intermolecular structure requires an assignment of OH frequencies to structural variables of the liquid, which is still a topic of considerable debate (6–10). Previous simulation studies have highlighted the role of local hydrogen-bonding coordinates, but have not provided a simple, unifying picture of dephasing for all time scales. We address both of these issues by performing time-resolved IR spectroscopy on water with 52-fs IR pulses, allowing detection of faster dynamics, and by developing an atomistic model that qualitatively reproduces experimental results, exposing the essential molecular features that control spectral diffusion.

The quantitative measure of spectral diffusion that is accessible by both experiment and simulation is the OH frequency correlation function  $C_{10}(\tau) = \langle \delta\omega_{10}(\tau)\delta\omega_{10}(0) \rangle$ . Here  $\delta\omega_{10}(\tau)$  is the difference between the instantaneous transition frequency and its time-averaged value.  $C_{10}(\tau)$  is the ensemble-averaged measure of the amplitude and time scales for the loss of memory of a given OH frequency. It can be extracted from a vibrational echo peak shift (PS) measurement if the frequency fluctuations are Gaussian and the pulses used in the experiment are shorter than the dynamics of interest (14–17).

In the PS measurement, three IR pulses, whose time delays can be adjusted with respect to each other, are focused into a sample to generate a new signal (Fig. 1C). The first two pulses ( $E_a$  and  $E_b$ ), separated in time by a delay  $\tau_1$ , form a spectral frequency comb with a spacing  $1/\tau_1$  that excites a spectral pattern of OH vibrations within the absorption line. Subsequent changes in hydrogen-bonding configurations cause OH spectral diffusion processes that gradually destroy this fringe pattern at a rate related to  $C_{10}(\tau)$  (Fig. 1B). After waiting for a time  $\tau_2$ , a third pulse ( $E_c$ ) stimulates the emission of a signal. We measure the integrated intensity of the ra-

diated signal as a function of the time delay  $\tau_1$ , for fixed values of the waiting time  $\tau_2$ . The PS is obtained by plotting the value of  $\tau_1$  that maximizes the integrated signal,  $\tau_1^*$ , as a function of  $\tau_2$ .

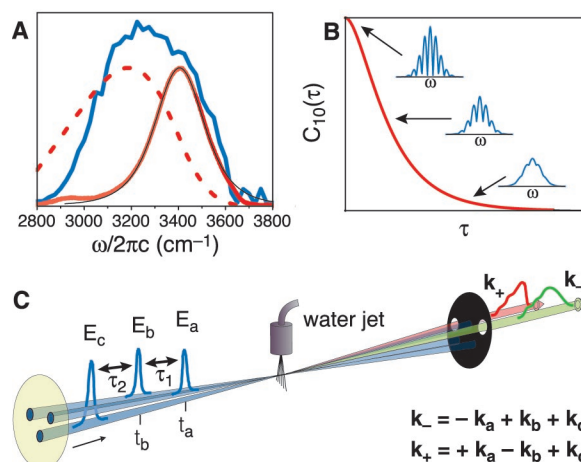
Our PS measurements used 52-fs IR pulses centered at  $3275\text{ cm}^{-1}$  ( $3.05\text{ }\mu\text{m}$ ), generated with a home-built, white-light-seeded, two-stage BBO/KNbO<sub>3</sub> optical parametric amplifier and compressed to second order at the sample by matching positive and negative material dispersion in the interferometer. These pulses have enough bandwidth to span both the fundamental transition ( $\nu = 1 \leftarrow 0$ ) and most of the anharmonically shifted  $\nu = 2 \leftarrow 1$  absorption (18) (Fig. 1A). The pulse length is shorter than the inverse of the line-width, ensuring that all relevant dynamics of the OH frequency are captured. The sample, approximately 1% HOD in D<sub>2</sub>O with a peak absorbance of 0.35 at  $3400\text{ cm}^{-1}$ , was continuously flowed as a 50- $\mu\text{m}$  path-length jet. This low concentration ensures that OH oscillators do not interact. A typical experimentally measured PS (Fig. 2A) decays from an initial value of  $\tau_1^*(0) = 28\text{ fs}$ , with time scales of 75 fs and 1.2 ps, and exhibits a damped oscillation that peaks at 150 fs. As observed in electronic PS measurements (19), the amplitude and phase characteristics of the pulse strongly influence the initial value and early decay time scale. In our experiment, these varied between 24 and 28 fs and 70 and 120 fs, respectively. The pulse characteristics slightly affect the depth of modulation of the oscillation, but the maximum consistently occurred at 150 fs. To include the amplitude and phase characteristics of the pulse in the modeling of a particular PS, a second harmonic, frequency-resolved, optically gated autocorrelation was recorded immediately after each PS measurement. Because we accounted for

finite pulse duration and chirp in air calculation, the extracted correlation function is independent of these pulse characteristics.

$C_{10}(\tau)$  was extracted from the PS measurements by an iterative procedure. We first compared the PS calculated from a trial correlation function to the experimental PS, and then repeatedly adjusted the amplitudes and time scales of the trial correlation function to improve the fit (Fig. 2A). The trial correlation function is composed of two overdamped and two underdamped oscillators, whose initial frequencies correspond to the time scales present in the PS. The calculation follows a formalism for a multilevel system coupled to a bath with arbitrary time scales (20), but neglects molecular reorientation. We explicitly include the pulse amplitude and phase and constraints to fit the linear absorption spectrum. It takes into account the ground and first two excited states of the HOD molecule. Harmonic scaling rules relate the frequency autocorrelation functions and transition dipole moments for the transitions between different levels. The correlation function extracted from the PS measurement (Fig. 2B, top) has the same qualitative features as the measured PS, though the relative amplitudes are different. The time scale for the initial decay is slightly shorter ( $\sim 60\text{ fs}$ ), and the oscillation is more prominent, peaking at 170 fs because of a small phase shift in the correlation function relative to the PS (15). The long time component, however, is nearly unchanged.

Decay time constants of roughly 0.1 and 1 ps in water have been observed or predicted from prior experimental and theoretical investigations. Previous IR transient hole-burning and IR PS experiments have measured decay times in the range of 0.5 to 1.0 ps. These have been interpreted in a number

**Fig. 1.** (A) The IR absorption spectrum of 1% HOD in D<sub>2</sub>O in the OH stretching region (solid red line) and the anharmonically shifted  $\nu = 2 \leftarrow 1$  induced absorption [dashed red line, taken from (18)], compared with the pulse spectrum (blue line). The absorption spectrum simulated from the extracted correlation function (black line) is superimposed on the experimental data. c, the speed of light. (B) A schematic representation of the decay of the spectral frequency comb of OH vibrations (blue curves), which occurs at a rate related to  $C_{10}(\tau)$  during the time period between the second and third pulses (16). (C) The experimental geometry used for the PS measurement. Three identical mid-IR laser pulses are focused into the sample in a triangle geometry, such that  $\tau_1$  is the time separation between pulses a and b ( $t_a - t_b$ ) and  $\tau_2$  is the time separation between the second and third pulses. The radiated signals are detected in the  $k_+$  and  $k_-$  wave vector geometries, which allows for precise determination of  $\tau_1^*$  because of symmetrical exchange of the a and b pulse ordering.





## REPORTS

of ways, including diffusive changes in the O–H···O hydrogen-bond distance  $R_{\text{OO}}$  (8, 9), and changes in coordination number or tetrahedral ordering about the HOD (10). Recent IR echo measurements have reported additional time constants of 30 fs (12) and 130 fs (13), the latter of which was assigned to the breaking of individual hydrogen bonds.

The observation of an oscillation in the PS demonstrates that the OH stretch in water is coupled to underdamped intermolecular coordinates of the liquid, in contrast to other liquids, in which intermolecular motions are overdamped. A recurrence in the correlation function was recently predicted by theoretical studies of water by Hynes and coworkers (6) and by Lawrence and Skinner (7), but has eluded previous experimental measurements because the IR pulses used in those experiments were too long. The time scale of the oscillation is consistent with that measured by solvation experiments and other optical methods. For instance, optical Kerr effect and depolarized Raman experiments have observed peaks in the low-frequency Raman spectrum of D<sub>2</sub>O at 400, 170, and 60 cm<sup>−1</sup>, and have assigned them to librations, translational displacement, and bending motion of the intermolecular hydrogen-bond coordinate, respectively (21). Simulations suggest that these coordinates involve the concerted motion of many molecules (5, 22). The recurrence at 170 fs observed in this experiment corresponds to a peak at 180 cm<sup>−1</sup> in the spectral density (Fig. 2B, inset), suggesting that it may arise from oscillatory motion of the intermolecular hydrogen-bond coordinate. The small amplitude of the spectral density at 400 cm<sup>−1</sup> shows that librations do not substantially contribute to the measured OH frequency fluctuations.

To connect our spectroscopic results to fluctuations of chemically relevant microscopic coordinates, we developed and simulated an atomistic model for the equilibrium vibrational dynamics of HOD in liquid D<sub>2</sub>O. We chose an intermolecular potential, the extended simple point charge model, that consists of pairwise interaction energies (23). Whereas conventional use of this potential disregards all intramolecular vibrations, we added the OH stretch as a single quantum-mechanical degree of freedom. In addition to intermolecular energetics, the vibrational Hamiltonian includes an anharmonic gas phase potential (24). This stretching motion is much faster than the relevant fluctuations in its surroundings, so we treated it adiabatically by solving the time-independent Schrödinger equation for fixed configurations of its aqueous environment. Molecular translations and rotations evolve according to Newton's equation of motion.

Our approach is similar in spirit to the models of Hynes and coworkers (6) and

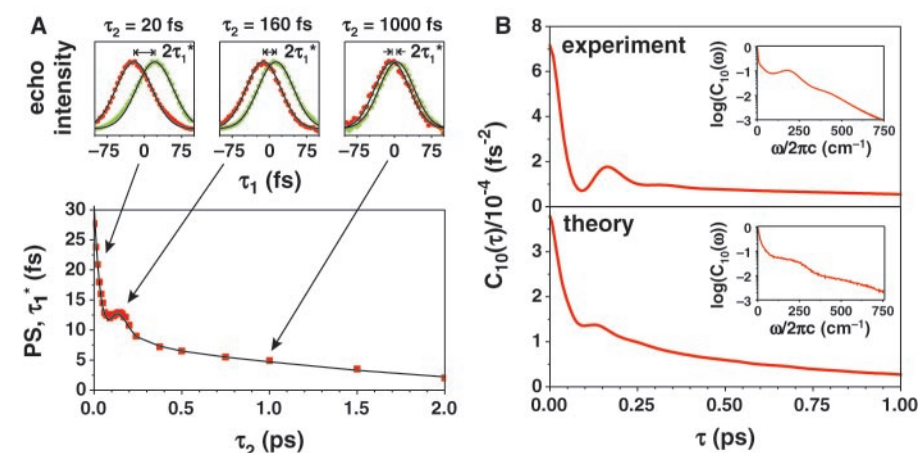


**Fig. 2.** (A) Top: Examples of experimentally measured normalized vibrational echoes of HOD in the  $k_+$  (red) and  $k_-$  (green) wave vector geometries for the indicated waiting times. For each  $\tau_2$ , the value of  $\tau_1^*$  is obtained by fitting both echoes with Gaussian functions to determine the time interval between peak positions. Bottom: The  $\tau_2$ -dependent, vibrational echo PS plotted with the best fit according to the procedure described in the text. (B) Comparison of  $C_{10}(\tau)$  extracted from the PS experiment (top) with the theoretical result predicted by the atomistic model (bottom). Inset: The cosine transform of each correlation function.

Lawrence and Skinner (7), but it is considerably simpler in its details. First, we neglected coupling of the vibrational coordinate to other intramolecular modes (25). Second, because the intermolecular potential is a slowly varying function of vibrational coordinate  $Q$ , we expanded it in powers of  $Q$ . Finally, because the solvent-induced energy shift is small compared to the gas-phase transition energy  $\hbar\omega_{10}^{(0)}$  (where  $\hbar$  is Planck's constant divided by  $2\pi$ ) we used perturbation theory to determine vibrational frequencies. We worked to second order in both the expansion and perturbation theory, but have found that first-order approximations are sufficient for qualitative accuracy. Intermolecular forces on the relatively massive oxygen atom, such as dispersion and short-ranged repulsion, act weakly on  $Q$ , so that first-order changes in the vibrational frequency are simply Stark shifts

$$\omega_{10} \approx \omega_{10}^{(0)} - \frac{z_H E}{\hbar} (\langle 1|Q|1 \rangle - \langle 0|Q|0 \rangle)$$

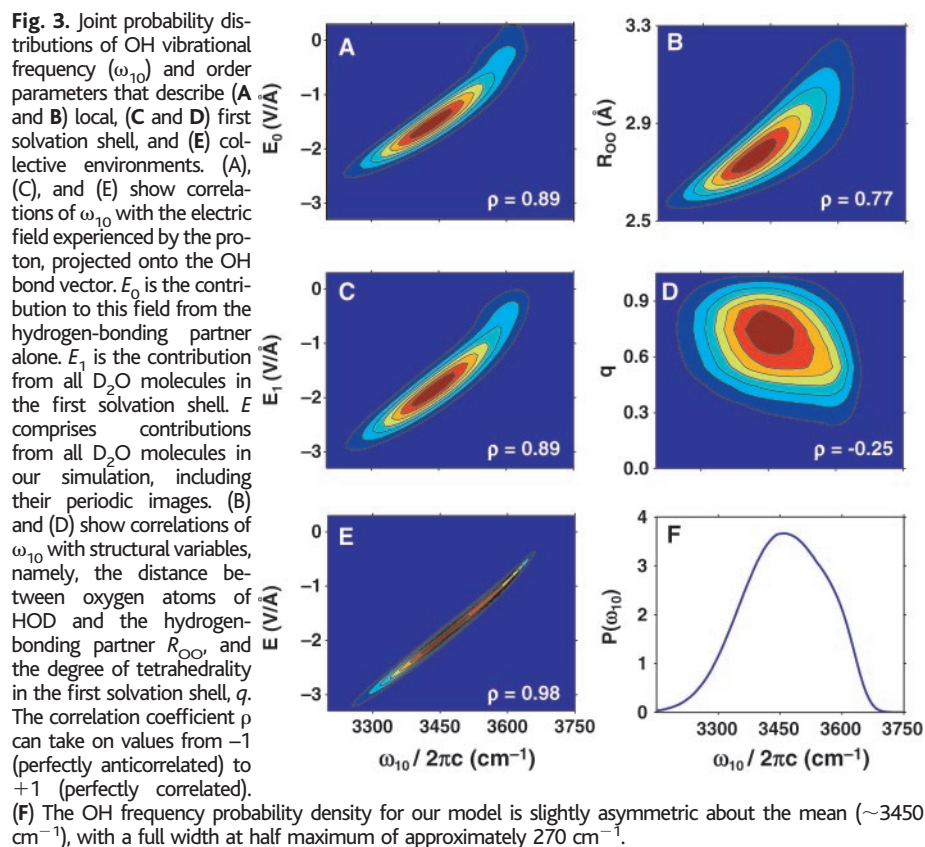
Here,  $|i\rangle$  represents eigenstate  $i$  of the unperturbed vibration,  $\omega$  is the OH vibrational frequency,  $z_H$  is the proton's charge, and  $E$  is the liquid's electric field, as experienced by the proton, projected onto the OH bond vector. To a good approximation, dynamics of  $\omega_{10}$  provide a direct measure of polarization fluctuations in the aqueous environment. The accuracy of such a simple picture is notable given the formally nonlocal and nonlinear dependence of frequency shifts on intermolecular forces. This observation, which was not apparent in more complicated approaches, greatly facilitates a molecular interpretation of the vibrational dephasing.

The frequency distribution (Fig. 3F) and autocorrelation function (Fig. 2B) obtained

from our model demonstrate that nothing essential is sacrificed in our simplifications. Indeed, our  $C_{10}(\tau)$  is nearly indistinguishable from that reported in (6) and (7). More importantly, it exhibits the same qualitative features as the result extracted from our PS measurements. Correlations decay initially with a time constant less than 100 fs, exhibit an oscillation that peaks near 150 fs, and decay at long times with a time constant of roughly 600 fs.

The Coulomb forces in our model are long-ranged, and we therefore expect collective motions to strongly influence frequency dynamics. Nonetheless, the strength of individual hydrogen bonds imparts a unique significance to the D<sub>2</sub>O molecule closest to the OH proton. The joint probability distribution of the electric field from this hydrogen-bonding partner,  $E_0$ , and vibrational frequency confirms this notion (Fig. 3A). Strong correlation between these two coordinates has been foreshadowed by others' results, which demonstrate correlations of  $\omega_{10}$  and the distance  $R_{\text{OO}}$  between oxygen atoms involved in the O–H···O hydrogen bond (6, 7). The correlations with  $R_{\text{OO}}$ , however, are weaker (Fig. 3B) than those between frequency and  $E_0$ , because  $E_0$  also depends on other geometrical features of the hydrogen bond. Although the importance of bond distance and angle has been noted previously, our model reveals that  $E_0$  is the single relevant combination of local coordinates.

Adding a description of first-solvation-shell structure does not improve upon the correlation obtained with  $E_0$  alone. We define  $E_1$  as the electric field generated by all four immediate neighbors of the HOD molecule. The joint distribution of  $E_1$  and  $\omega_{10}$  (Fig. 3C) shows a correlation that is no stronger than



that between  $\omega_{10}$  and  $E_0$ . The interpretation that frequency shifts reflect transitions between a few distinct first-shell arrangements, however, would require that the opposite be true. We have tested this idea more explicitly by examining the relationship between  $\omega_{10}$  and an order parameter  $q$  that describes the degree of local tetrahedral structure (26, 27). The vibrational frequency is only weakly related to tetrahedrality (Fig. 3D).

Continuing to add electrostatic contributions from more distant solvation shells, we find no significant improvement in correlation until all molecules in our simulation cell (and their periodic images) are included (Fig. 3E). Beyond  $E_0$ , the driving force for vibrational dynamics is indeed collective. This situation is reminiscent of solvation dynamics experiments, in which the relaxation of electronic excited states is modulated by long-wavelength fluctuations in solvent polarization (28). The similarity suggests that reduced dielectric descriptions of water appropriate for solvation dynamics (29) added to a detailed picture of local hydrogen bonding may be appropriate for our experiment (30).

The dynamics of these order parameters, illustrated through their time correlation functions in Fig. 4, further reveal the origins of frequency fluctuations. The most marked is the resemblance of the  $E_0$  autocorrelation function to  $C_{10}(\tau)$  at short times. In particular, the oscillation at 150 fs is prominent. This

feature appears to be a signature of local relaxation. It is also observed in the dynamics of  $R_{OO}$ , indicating that dephasing of hydrogen-bond stretching is an important component of frequency relaxation at short times. The relaxation of collective electrostatic contributions (excluding  $E_0$ ) mirrors the dielectric dispersion of water, with a beat around 60 fs typically assigned to librations (2). All of the time correlation functions presented in Fig. 4 decay asymptotically on time scales of  $\sim 0.6$  to 1 ps. As a consequence, the long-time decay of frequency correlations cannot be associated with a single specific motion of individual molecules. Instead, it reflects a variety of relaxation mechanisms, including collective rearrangement of the hydrogen-bond network, as well as density and polarization fields, on length scales greater than a molecular diameter.

Our study reveals that the vibrational dynamics observed in IR spectroscopy are dominated by underdamped displacement of the hydrogen-bond coordinate at very short times ( $< 200$  fs). This local picture does not apply at longer times, where configurational changes, including the breaking and forming of hydrogen bonds, involve the concerted motions of many molecules. Many spectroscopic techniques have probed this collective, though still microscopic, relaxation. Understanding the more detailed molecular dynamics of liquid water has long relied on numer-

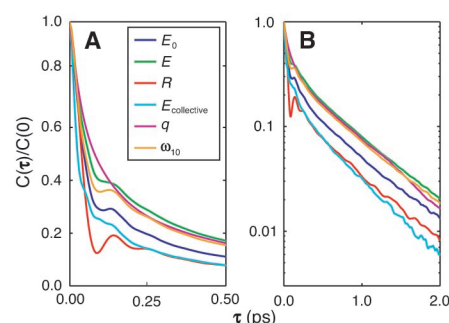


**Fig. 4.** (A and B) Normalized time correlation functions  $C(\tau)/C(0)$  of the order parameters examined in Fig. 3 and of the collective electric field (excluding contributions from the hydrogen-bonding partner,  $E_{\text{collective}} = E - E_0$ ). The logarithmic vertical scale in (B) highlights the uniformity of the relaxation at long times.

ical simulations of empirical models. By revealing a specific intermolecular motion, namely, stretching of a single hydrogen bond, our PS measurement brings the ultrafast IR spectroscopy of liquid water into this microscopic realm.

#### References and Notes

- W. Jarzeba, G. C. Walker, A. E. Johnson, M. A. Kahlow, P. F. Barbara, *J. Phys. Chem.* **92**, 7039 (1988).
- R. Jimenez, G. R. Fleming, P. V. Kumar, M. Maroncelli, *Nature* **369**, 471 (1994).
- M. J. Lang, X. J. Jordanides, X. Song, G. R. Fleming, *J. Chem. Phys.* **110**, 5884 (1999).
- F. H. Stillinger, *Adv. Chem. Phys.* **31**, 1 (1975).
- I. Ohmine, H. Tanaka, *Chem. Rev.* **93**, 2545 (1993).
- R. Rey, K. B. Moller, J. T. Hynes, *J. Phys. Chem. A* **106**, 11993 (2002).
- C. P. Lawrence, J. L. Skinner, *J. Chem. Phys.* **118**, 264 (2003).
- G. M. Gale et al., *Phys. Rev. Lett.* **82**, 1068 (1999).
- S. Woutersen, H. J. Bakker, *Phys. Rev. Lett.* **83**, 2077 (1999).
- R. Laenen, K. Simeonidis, A. Laubereau, *J. Phys. Chem. B* **106** (2002).
- J. Stenger, D. Madsen, P. Hamm, E. T. J. Nibbering, T. Elsaesser, *J. Phys. Chem. A* **106**, 2341 (2002).
- J. Stenger, D. Madsen, P. Hamm, E. T. J. Nibbering, T. Elsaesser, *Phys. Rev. Lett.* **87**, 027401 (2001).
- S. Yermenko, M. S. Pshenichnikov, D. A. Wiersma, *Chem. Phys. Lett.* **369**, 107 (2003).
- M. Cho et al., *J. Phys. Chem.* **100**, 11944 (1996).
- T. Joo, Y. Jia, J.-Y. Yu, M. J. Lang, G. R. Fleming, *J. Chem. Phys.* **104**, 6089 (1996).
- W. P. de Boeij, M. S. Pshenichnikov, D. A. Wiersma, *Annu. Rev. Phys. Chem.* **49**, 99 (1998).
- A. Piryatinski, C. P. Lawrence, J. L. Skinner, *J. Chem. Phys.* **118** (2003).
- H. J. Bakker et al., *J. Chem. Phys.* **116**, 2592 (2002).
- K. Ohta, D. Larsen, M. Yang, G. R. Fleming, *J. Chem. Phys.* **114**, 8020 (2001).
- J. Sung, R. J. Silbey, *J. Chem. Phys.* **115**, 9266 (2001).
- E. W. Castner Jr., Y. J. Chang, Y. C. Chu, G. E. Walrafen, *J. Chem. Phys.* **102**, 653 (1995).
- M. Cho, G. R. Fleming, S. Saito, I. Ohmine, R. M. Stratt, *J. Chem. Phys.* **100**, 6672 (1994).
- H. J. C. Berendsen, J. R. Grigera, T. P. Straatsma, *J. Phys. Chem.* **91**, 6269 (1987).
- J. R. Reimers, R. O. Watts, *Mol. Phys.* **52**, 357 (1984).
- D. W. Oxtoby, *Adv. Chem. Phys.* **40**, 1 (1979).
- J. R. Errington, P. G. Debenedetti, *Nature* **409**, 318 (2001).
- The tetrahedrality  $q$  quantifies the degree of tetrahedral order from molecules in the first solvation shell around HOD. It is defined by

$$q = 1 - \frac{3}{8} \sum_{j=1}^3 \sum_{k=j+1}^4 (\hat{r}_{oj} \cdot \hat{r}_{ok} + \frac{1}{3})^2$$

Here  $\hat{r}_{oj}$  and  $\hat{r}_{ok}$  are unit vectors pointing from the oxygen of HOD to the oxygen atom of first-shell molecules numbered  $j$  and  $k$ , respectively. It is normalized to unity if the solvation shell forms a perfect tetrahedron, and its average value is zero in the gas

phase where there is no preferred intermolecular orientational ordering.

28. B. Bagchi, D. W. Oxtoby, G. R. Fleming, *Chem. Phys.* **86**, 257 (1984).
29. X. Song, D. Chandler, R. A. Marcus, *J. Phys. Chem.* **100**, 11954 (1996).
30. Y. Georgievskii, R. A. Marcus, *J. Phys. Chem. A* **105**, 2281 (2001).
31. We thank J. L. Skinner for many helpful conversations and both J. L. Skinner and J. T. Hynes for sending

preprints of their work. Supported by Basic Energy Sciences of the U.S. Department of Energy (grant no. DE-FG02-99ER14988), the NSF Laser Research Facility at MIT (grant no. CHE-0111370), and the David and Lucile Packard Foundation. P.L.G. is an MIT Science Fellow. J.J.L. thanks the U.S. Department of Defense for a National Defense Science and Engineering Graduate fellowship.

27 May 2003; accepted 6 August 2003

# Generation of Megawatt Optical Solitons in Hollow-Core Photonic Band-Gap Fibers

Dimitre G. Ouzounov,<sup>1</sup> Faisal R. Ahmad,<sup>1</sup> Dirk Müller,<sup>2</sup>  
Natesan Venkataraman,<sup>2</sup> Michael T. Gallagher,<sup>2</sup>  
Malcolm G. Thomas,<sup>1</sup> John Silcox,<sup>1</sup> Karl W. Koch,<sup>2</sup>  
Alexander L. Gaeta<sup>1\*</sup>

The measured dispersion of a low-loss, hollow-core photonic band-gap fiber is anomalous throughout most of the transmission band, and its variation with wavelength is large compared with that of a conventional step-index fiber. For an air-filled fiber, femtosecond self-frequency-shifted fundamental solitons with peak powers greater than 2 megawatts can be supported. For Xe-filled fibers, nonfrequency-shifted temporal solitons with peak powers greater than 5.5 megawatts can be generated, representing an increase in the power that can be propagated in an optical fiber of two orders of magnitude. The results demonstrate a unique capability to deliver high-power pulses in a single spatial mode over distances exceeding 200 meters.

Fiber propagation of high-power laser pulses in a single spatial mode is important for many scientific and technological applications, such as fiber lasers and amplifiers, multiphoton spectroscopy, and photodynamic therapy. In a conventional fiber, which operates via total internal reflection, optical nonlinearities impose a severe limitation on the ability to maintain the fidelity (e.g., pulse duration and peak power) of ultrashort pulses and thus restrict the use of pulses to energies no higher than the nanjoule level (1, 2). Recent development (3, 4) of photonic band-gap fibers (PBGFs) has created a new paradigm in which light is guided via diffraction, rather than by total internal reflection, and thus enables fiber designs in which the light field is confined to an air, or even a vacuum, core. In such fibers, optical nonlinearities are reduced by more than a factor of 1000 compared with silica-core fibers, and delivery of microjoule femtosecond pulses is possible. The total dispersion of these fibers is dominated by the waveguide disper-

sion, which in most cases is anomalous [i.e.,  $D = -(\lambda/c)d^2n/d\lambda^2 > 0$ , where  $\lambda$  is the wavelength,  $c$  is the speed of light in vacuum, and  $n$  is the effective refractive index of the waveguide mode] and has a large slope within the transmission gap that, together with the extremely low nonlinearity, allows for the generation of high-power optical solitons. By filling the holes of the fiber with other gases, such fibers could also find applications in a number of other fields, greatly extending the interaction lengths for atomic and molecular spectroscopy or for nonlinear optical processes (5). In addition, because the scattering losses of PBGFs could be theoretically 1000 times less than that of conventional fibers, it should impact telecommunications and quantum information applications where minimization of losses is critical.

Our low-loss PBGF (6) was designed to produce a transmission band in the near-infrared spectral range (Fig. 1). The cladding region consists of a triangular array of air holes that run along the entire fiber length (Fig. 1A), constituting a two-dimensional (2D) photonic crystal that confines the light to the central air region, that is, the core of the fiber. The operation of a PBGF relies on the existence of a photonic band gap rather than on total internal reflection,

which makes guiding in regions with lower refractive index possible. This fiber was fabricated by using the standard stack-and-draw method (7). The diameter of the core is 12.7  $\mu\text{m}$ , the pitch between the air holes is 4.7  $\mu\text{m}$ , and the air-filling fraction is 0.94. This fiber has the lowest reported minimum attenuation for a PBGF (13 dB/km at 1500 nm) (6, 8), which is 100 times lower than that of previously fabricated designs (5). The attenuation spectrum (Fig. 1B) shows a fiber transmission window, which spans the wavelength range between 1395 and 1510 nm.

The dispersion of the group velocity of the fiber was measured with the use of a time-delay technique (9, 10) [Supporting Online Material (SOM) Text] that uses a tunable femtosecond source and a two-photon detector (11). For this fiber (Fig. 1C), the zero-dispersion wavelength is 1425 nm, and over most of the transmission band the dispersion is anomalous. As evidenced by the large slope of the measured data, the third-order dispersion of the guided mode in air is considerably greater than that of a conventional silica fiber at these wavelengths, and thus the dispersion can be attributed almost entirely to the waveguide dispersion associated with the structure. These large values of the dispersion (normal at the shorter-wavelength band edge and anomalous at the longer-wavelength band edge) is inherent from the Kramers-Kronig relations to any optical structure that has relatively sharp transmission features, which typically leads to a zero-dispersion point at the center of the gap. However, as is observed with step-index silica fibers (12) and hollow metallic waveguides (13), the 1D waveguiding produces a supplementary anomalous contribution to the dispersion, resulting in the observed shift to the short-wavelength band edge. Thus, the existence of a range in the transmission gap where the dispersion is large and anomalous appears to be a generic feature of these types of PBGFs. The theoretical prediction based on the full vector-Maxwell equations for the dispersion of the fundamental air-core mode is consistent with the experimental observations near the center of the transmission band but deviates near the edges. Further theoretical analysis will be required to understand the lack of agreement at the band edges.

<sup>1</sup>School of Applied and Engineering Physics, Cornell University, Ithaca, NY 14853, USA. <sup>2</sup>Sullivan Park, Corning Incorporated, Corning, NY 14831, USA.

\*To whom correspondence should be addressed. E-mail: a.gaeta@cornell.edu